

IEEE TRANSACTIONS ON GEOSCIENCE AND REMOTE SENSING

A PUBLICATION OF THE IEEE GEOSCIENCE AND REMOTE SENSING SOCIETY



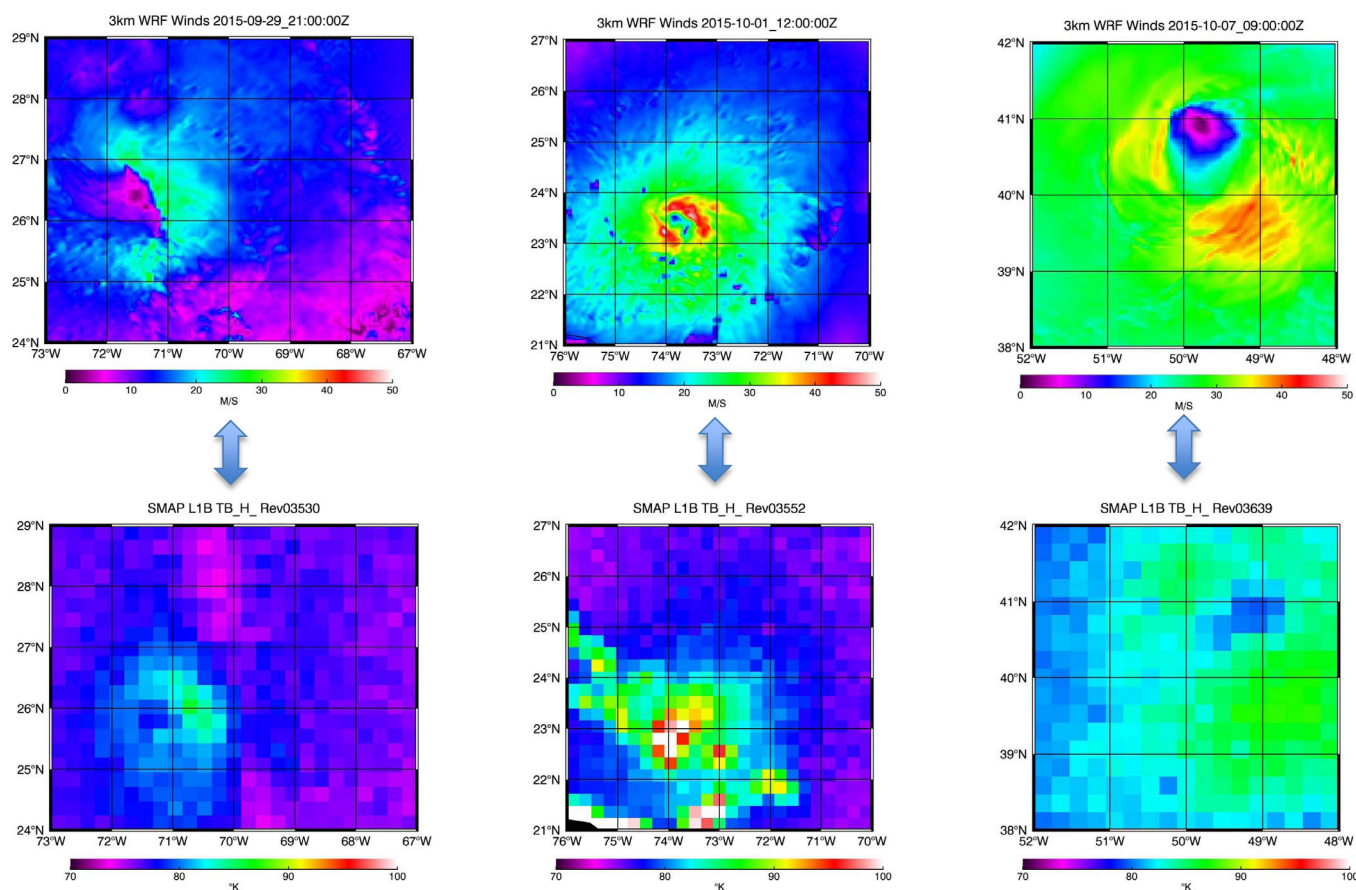
DECEMBER 2016

VOLUME 54

NUMBER 12

IGRSD2

(ISSN 0196-2892)



The SMAP data have a good correlation with the ocean surface wind speeds of Hurricane Joaquin in 2015 with generally higher brightness temperatures for higher wind speeds. (Top) APSU surface winds of Joaquin on Sept. 29 at 21 UT, Oct. 1 at 12 UT, and Oct. 7 at 9 UT. (Bottom) Corresponding SMAP brightness temperature data for horizontal polarization from three passes.

IEEE TRANSACTIONS ON GEOSCIENCE AND REMOTE SENSING

A PUBLICATION OF THE IEEE GEOSCIENCE AND REMOTE SENSING SOCIETY



DECEMBER 2016

VOLUME 54

NUMBER 12

IGRSD2

(ISSN 0196-2892)

PAPERS

Atmosphere

- Uncertainty in Fengyun-3C Microwave Humidity Sounder Measurements at 118 GHz With Respect to Simulations From GPS RO Data *Z. Qin and X. Zou* 6907

Oceans

- Multisite Remote Sensing for Tsunami-Induced Waves
. *G. Chen, J. Wang, C. Wu, X. Huang, D. Zhong, H. Qi, L. Huang, and Y. Li* 7177

Vegetation and Land

- Convenient Measurement and Modified Model for Broadleaf Permittivity
. *Y. Zhang, Q. Liu, Y. Du, L. Yang, Y. Du, B. Cao, and L. Tan* 6986
- Snow Depth Retrieval Based on a Multifrequency Dual-Polarized Passive Microwave Unmixing Method From Mixed Forest Observations *L. Gu, R. Ren, and X. Li* 7279
- An Iterative Learning Framework for Multimodal Chlorophyll-a Estimation *J. C. Davila and M. B. Zaremba* 7299
- Fractional Vegetation Cover Estimation Method Through Dynamic Bayesian Network Combining Radiative Transfer Model and Crop Growth Model. *X. Wang, K. Jia, S. Liang, and Y. Zhang* 7442

Electromagnetics

- In-Loop Transient Electromagnetic Responses With Induced Polarization Effects of Deep-Sea Hydrothermal Deposits. *H. Jang, H. J. Kim, and M. J. Nam* 7272

Hyperspectral Data Processing

- Joint Anomaly Detection and Spectral Unmixing for Planetary Hyperspectral Images
. *S. Nakhostin, H. Clenet, T. Corpetti, and N. Courty* 6879
- Hyperspectral Feature Extraction Using Total Variation Component Analysis.
. *B. Rasti, M. O. Ulfarsson, and J. R. Sveinsson* 6976
- Laplacian Regularized Collaborative Graph for Discriminant Analysis of Hyperspectral Imagery *W. Li and Q. Du* 7066
- Set-to-Set Distance-Based Spectral-Spatial Classification of Hyperspectral Images
. *T. Lu, S. Li, L. Fang, L. Bruzzone, and J. A. Benediktsson* 7122
- Dictionary Learning for Promoting Structured Sparsity in Hyperspectral Compressive Sensing.
. *L. Zhang, W. Wei, Y. Zhang, C. Shen, A. van den Hengel, and Q. Shi* 7223

(Contents Continued on Page 6846)

Multiband Image Fusion Based on Spectral Unmixing	7236
. <i>Q. Wei, J. Bioucas-Dias, N. Dobigeon, J.-Y. Tourneret, M. Chen, and S. Godsill</i>	
Class-Specific Sparse Multiple Kernel Learning for Spectral–Spatial Hyperspectral Image Classification.	7351
. <i>T. Liu, Y. Gu, X. Jia, J. A. Benediktsson, and J. Chanussot</i>	
Probabilistic Fusion of Pixel-Level and Superpixel-Level Hyperspectral Image Classification.	7416
. <i>S. Li, T. Lu, L. Fang, X. Jia, and J. A. Benediktsson</i>	
Constant SNR, Rate Control, and Entropy Coding for Predictive Lossy Hyperspectral Image Compression	7431
. <i>M. Conoscenti, R. Coppola, and E. Magli</i>	
Image Processing and Analysis	
On-Orbit Spatial Quality Evaluation and Image Restoration of FengYun-3C/MERSI.	6847
. <i>M. Min, G. Cao, N. Xu, Y. Bai, S. Jiang, X. Hu, L. Dong, J. Guo, and P. Zhang</i>	
Iterative Classifiers Combination Model for Change Detection in Remote Sensing Imagery	6997
. <i>R. Hedjam, M. Kalacska, M. Mignotte, H. Ziaei Nafchi, and M. Cheriet</i>	
Remote Sensing Image Stripe Noise Removal: From Image Decomposition Perspective	7018
. <i>Y. Chang, L. Yan, T. Wu, and S. Zhong</i>	
An Inquiry on Contrast Enhancement Methods for Satellite Images.	7044
. <i>J.-L. Lisani, J. Michel, J.-M. Morel, A. B. Petro, and C. Sbert</i>	
Coupled Dictionary Learning for Change Detection From Multisource Data	7077
. <i>M. Gong, P. Zhang, L. Su, and J. Liu</i>	
Hierarchical and Adaptive Phase Correlation for Precise Disparity Estimation of UAV Images	7092
. <i>J. Li, Y. Liu, S. Du, P. Wu, and Z. Xu</i>	
An Integrated Framework for the Spatio–Temporal–Spectral Fusion of Remote Sensing Images.	7135
. <i>H. Shen, X. Meng, and L. Zhang</i>	
An Iterative Interpolation Deconvolution Algorithm for Superresolution Land Cover Mapping.	7210
. <i>F. Ling, G. M. Foody, Y. Ge, X. Li, and Y. Du</i>	
Discriminative-Dictionary-Learning-Based Multilevel Point-Cluster Features for ALS Point-Cloud Classification.	7309
. <i>Z. Zhang, L. Zhang, X. Tong, B. Guo, L. Zhang, and X. Xing</i>	
A Bilevel Scale-Sets Model for Hierarchical Representation of Large Remote Sensing Images.	7366
. <i>Z. Hu, Q. Li, Q. Zou, Q. Zhang, and G. Wu</i>	
Learning Rotation-Invariant Convolutional Neural Networks for Object Detection in VHR Optical Remote Sensing Images	7405
. <i>G. Cheng, P. Zhou, and J. Han</i>	
Microwave Radiometry	
Active–Passive Disaggregation of Brightness Temperatures During the SMAPVEX12 Campaign	6859
. <i>D. J. Leroux, N. N. Das, D. Entekhabi, A. Colliander, E. G. Njoku, R. S. Dunbar, and S. H. Yueh</i>	
Sensitivity of Ocean Surface Salinity Measurements From Spaceborne L-Band Radiometers to Ancillary Sea Surface Temperature.	7105
. <i>T. Meissner, F. J. Wentz, J. Scott, and J. Vazquez-Cuervo</i>	
Retrieving Profile Temperatures in a Frozen Topsoil Near the TFS, Alaska, Based on SMOS Brightness Temperatures at the 1.4-GHz Frequency.	7331
. <i>V. L. Mironov, K. V. Muzalevskiy, and Z. Ruzicka</i>	
SMAP L-Band Passive Microwave Observations of Ocean Surface Wind During Severe Storms	7339
. <i>S. H. Yueh, A. G. Fore, W. Tang, A. Hayashi, B. Stiles, N. Reul, Y. Weng, and F. Zhang</i>	
Evaluating Multispectral Snowpack Reflectivity With Changing Snow Correlation Lengths	7378
. <i>D.-H. Kang, A. P. Barros, and E. J. Kim</i>	
Combined Active/Passive Retrievals of Ocean Vector Wind and Sea Surface Salinity With SMAP.	7396
. <i>A. G. Fore, S. H. Yueh, W. Tang, B. W. Stiles, and A. K. Hayashi</i>	
Radar Systems	
Probabilistic Attenuation Correction in a Networked Radar Environment.	6930
. <i>S. Shimamura, V. Chandrasekar, T. Ushio, G. Kim, E. Yoshikawa, and H. Chen</i>	
Inverting for Maritime Environments Using Proper Orthogonal Bases From Sparsely Sampled Electromagnetic Propagation Data	7166
. <i>V. Fountoulakis and C. Earls</i>	
Efficient Stolt Migration for Large Nonuniform Single Borehole Radar Surveys.	7250
. <i>H. Yang, T. Li, N. Li, Z. He, and Q. H. Liu</i>	
Mitigation of Reflection Symmetry Assumption and Negative Power Problems for the Model-Based Decomposition.	7261
. <i>H. Li, J. Chen, Q. Li, G. Wu, and J. Chen</i>	
A Dual-Wavelength Radar Technique to Detect Hydrometeor Phases	7292
. <i>L. Liao and R. Meneghini</i>	

Dynamical Properties of Sea Surface Microwave Backscatter at Low-Incidence: Correlation Time and Doppler Shift	<i>O. Boiso</i> t, <i>L. Amarouche</i> , <i>J.-C. Lalaurie</i> , and <i>C.-A. Guérin</i>	7385
Synthetic Aperture Radar		
Three-Dimensional Deformation Monitoring of Urban Infrastructure by Tomographic SAR Using Multitrack TerraSAR-X Data Stacks	<i>S. Montazeri</i> , <i>X. X. Zhu</i> , <i>M. Eineder</i> , and <i>R. Bamler</i>	6868
Urban Damage Level Mapping Based on Scattering Mechanism Investigation Using Fully Polarimetric SAR Data for the 3.11 East Japan Earthquake	<i>S.-W. Chen</i> , <i>X.-S. Wang</i> , and <i>M. Sato</i>	6919
Motion Errors and Compensation for Bistatic Forward-Looking SAR With Cubic-Order Processing	<i>W. Pu</i> , <i>J. Wu</i> , <i>Y. Huang</i> , <i>W. Li</i> , <i>Z. Sun</i> , <i>J. Yang</i> , and <i>H. Yang</i>	6940
Probabilistic Flood Mapping Using Synthetic Aperture Radar Data	<i>L. Giustarini</i> , <i>R. Hostache</i> , <i>D. Kavetski</i> , <i>M. Chini</i> , <i>G. Corato</i> , <i>S. Schlaffer</i> , and <i>P. Matgen</i>	6958
SAR Observation and Numerical Simulation of Mountain Lee Waves Near Kuril Islands Forced by an Extratropical Cyclone	<i>Q. Xu</i> , <i>X. Li</i> , <i>S. Bao</i> , and <i>L. J. Pietrafesa</i>	7157
Imaging the Internal Structure of an Alpine Glacier via L-Band Airborne SAR Tomography	<i>S. Tebaldini</i> , <i>T. Nagler</i> , <i>H. Rott</i> , and <i>A. Heilig</i>	7197
Three-Dimensional Variational Assimilation of InSAR PWV Using the WRFDA Model	<i>P. Mateus</i> , <i>R. Tomé</i> , <i>G. Nico</i> , and <i>J. Catalão</i>	7323
Global Navigation Satellite System		
Maximally Using GPS Observation for Water Vapor Tomography	<i>Y. Yao</i> and <i>Q. Zhao</i>	7185
Lidar Systems		
Adaptive Estimation of the Stable Boundary Layer Height Using Combined Lidar and Microwave Radiometer Observations	<i>U. Saeed</i> , <i>F. Rocadenbosch</i> , and <i>S. Crewell</i>	6895
Automatic Parameter Selection for Intensity-Based Registration of Imagery to LiDAR Data	<i>E. G. Parmehr</i> , <i>C. S. Fraser</i> , and <i>C. Zhang</i>	7032
A Combined Rotational Raman–Rayleigh Lidar for Atmospheric Temperature Measurements Over 5–80 km With Self-Calibration	<i>Y. Li</i> , <i>X. Lin</i> , <i>S. Song</i> , <i>Y. Yang</i> , <i>X. Cheng</i> , <i>Z. Chen</i> , <i>L. Liu</i> , <i>Y. Xia</i> , <i>J. Xiong</i> , <i>S. Gong</i> , and <i>F. Li</i>	7055
A Fuzzy Mean-Shift Approach to Lidar Waveform Decomposition	<i>Q. Li</i> , <i>S. Ural</i> , <i>J. Anderson</i> , and <i>J. Shan</i>	7112
Satellite Systems		
Impact of Assimilation of MADRAS Geophysical Parameters on Short Range WRF Model Forecasts	<i>A. W. Khan</i> , <i>P. Kumar</i> , and <i>A. K. Varma</i>	6970
VIIRS Reflective Solar Band Radiometric and Stability Evaluation Using Deep Convective Clouds	<i>T. Chang</i> , <i>X. Xiong</i> , and <i>Q. Mu</i>	7009
Development of Prototype Algorithms for Quantitative Precipitation Nowcasts From AMI Onboard the GEO-KOMPSAT-2A Satellite	<i>S. Hong</i> , <i>D.-B. Shin</i> , <i>B. Park</i> , and <i>D. So</i>	7149

2016 INDEX. Available online at <http://ieeexplore.ieee.org>

About the Cover: The cover illustrates the SMAP radiometer brightness temperature (T_B) data for Hurricane Joaquin in 2015. The bottom panels illustrate the SMAP T_B data for horizontal polarization from revs 3530A, 3552D, and 3639D. The upper panels illustrate the corresponding 3-km resolution APSU surface winds of Joaquin on Sept. 29, Oct. 1, and Oct. 7. The SMAP T_B data from rev 3530A have indicated generally higher T_B s for higher wind speeds. The APSU winds for the SMAP pass on Oct. 1, 2015 have exceeded 40 m/s, and the SMAP T_B s tend to have an increasing trend from far away to near the eye. On 7 October 2015, Joaquin became an extra-tropical storm. Its eye became quite large, reaching about 100 km in diameter. The SMAP T_B data reveal similar spatial patterns, and the hurricane eye can now be resolved by the SMAP radiometer. For more information please see “SMAP L-Band Passive Microwave Observations of Ocean Surface Wind During Severe Storms,” by Yueh *et al.*, which begins on page 7339.